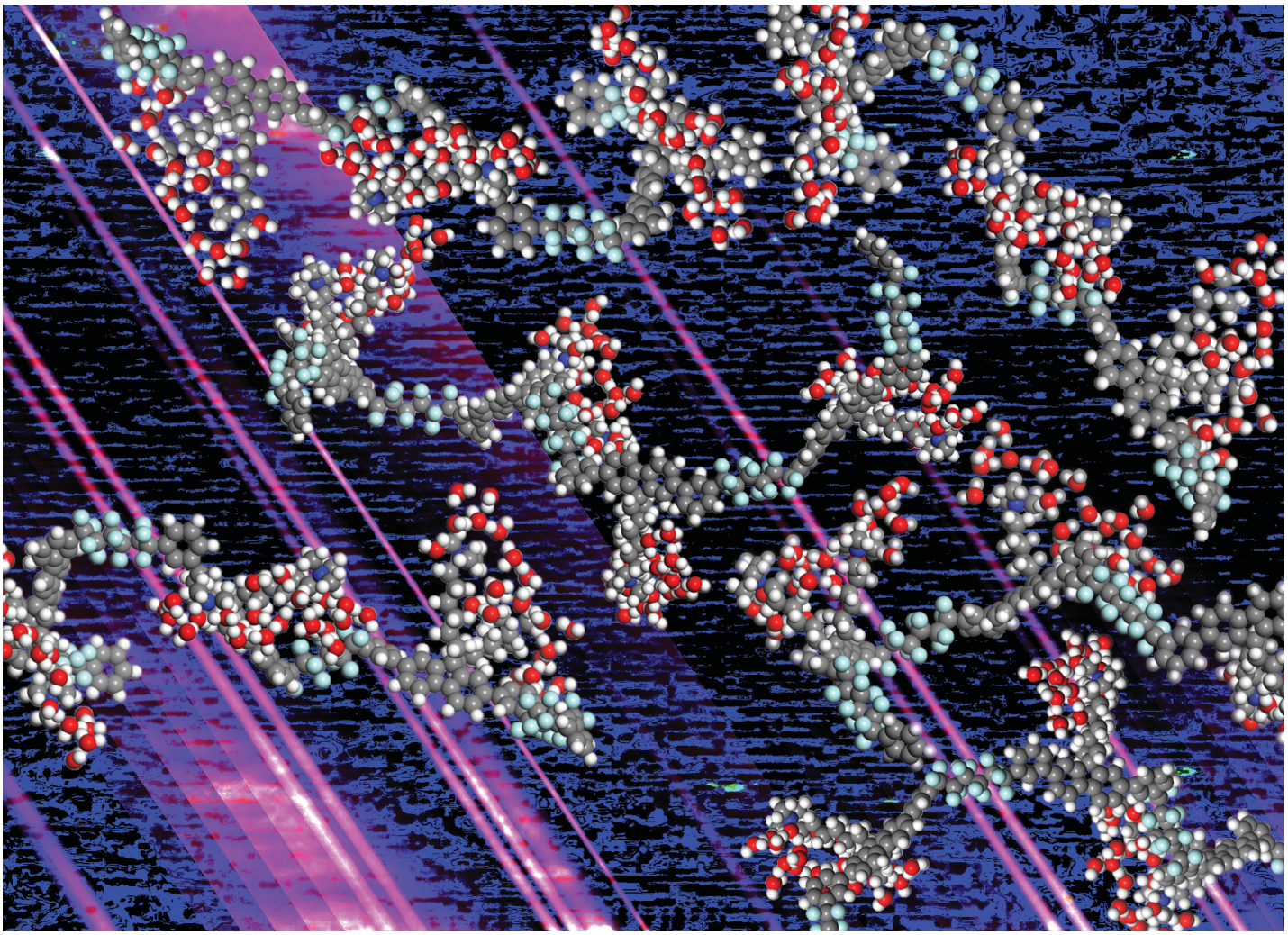

Showcasing research from the Junji Inukai group, Clean Energy Research Center, University of Yamanashi, Japan

Various states of water species in an anion exchange membrane characterized by Raman spectroscopy under controlled temperature and humidity

The Inukai group investigates the structure and dynamics of water in electrolyte membranes, especially in running fuel cells. The vibrational spectra of an anion exchange membrane and resident water molecules were obtained by Raman spectroscopy for the first time. Water interacting with water, water interacting with OH^-, non-H-bonded OH in water, and isolated OH^- were clearly distinguishable with the aid of DFT calculations. This work helps promote the development of non-PGM fuel cells and water electrolysers.

As featured in:

See Junji Inukai *et al.*, *Phys. Chem. Chem. Phys.*, 2024, **26**, 1658.

ROYAL SOCIETY OF CHEMISTRY

rsc.li/pccp

Registered charity number: 207890

PCCP Owner Societies

PCCP

ROYAL SOCIETY OF CHEMISTRY

PAPER

View Article Online
View Journal | View Issue

Cite this: *Phys. Chem. Chem. Phys.*, 2024, **26**, 1658

Various states of water species in an anion exchange membrane characterized by Raman spectroscopy under controlled temperature and humidity†

Solomon Wekesa Wakolo,[a] Donald A. Tryk,[b] Hiromichi Nishiyama,‡[b] Kenji Miyatake,[bcd] Akihiro Iiyama[b] and Junji Inukai *[bc]

Received 31st July 2023,
Accepted 11th November 2023

DOI: 10.1039/d3cp03660j

rsc.li/pccp

Anion exchange membrane fuel cells (AEMFCs) hold the key to future mass commercialisation of fuel cell technology, even though currently, AEMFCs perform less optimally than proton exchange membrane fuel cells (PEMFCs). Unlike PEMFCs, AEMFCs have demonstrated the capability to operate independently of Pt group metal-based catalysts. Water characterization inside the membrane is one factor that significantly influences the performance of AEMFCs. In this paper, different water species inside an anion exchange membrane (AEM), QPAF-4, developed at the University of Yamanashi, were studied for the first time using micro-Raman spectroscopy. Spectra of pure water, alkaline solutions, and calculations based on density functional theory were used to identify the water species in the AEM. The OH stretching band was deconvoluted into nine unique Gaussian bands. All the hydrogen-bonded OH species increased steadily with increasing humidity, while the CH and non-H-bonded OH remained relatively constant. These results confirm the viability of micro-Raman spectroscopy in studying the various water-related species in AEMs. The availability of this technique is an essential prerequisite in improving the ionic conductivity and effectively solving the persisting durability challenge facing AEMFCs, thus hastening the possibility of mass commercialisation of fuel cells.

1. Introduction

With the growing urgency to address global warming, curbing emissions from human activity is becoming increasingly necessary. Fuel cell technology is considered an integral part of an overall effective solution to this problem. Not only is the system energy efficient, with no production of CO_2, but the technology also has the added benefits of quietness and rapid refuelling. Silence and quick refuelling are especially attractive for automobile use.[1–4] In the case of portable applications such as in the automotive industry, proton exchange membrane fuel cells (PEMFCs) offer the highest power density, efficiency, and durability. However, their dependency on Pt has necessitated intensified research on anion exchange membrane fuel cells (AEMFCs). AEMFCs operate in the same temperature range but can potentially be independent of Pt-group metal-based catalysts. AEMs are also alkaline by definition, allowing for cheaper cell components because of the reduced corrosiveness.[4–6] Recently, Douglin *et al.*[6] demonstrated that, at high temperatures (110 °C), an AEMFC yielded better performance values than those reported for PEMFCs at the same temperature. Combining the cheaper catalysts, cheaper cell building materials and reported excellent high-temperature performance can dramatically lower overall fuel cell cost per kilowatt and enable widespread technology commercialisation.

One of the biggest challenges in commercialising AEMFCs has always been the anion exchange membrane (AEM).[3] A viable fuel cell membrane must display high ion conductivity ($\geq 100 \times 10^{-3}$ S cm^{-1}[7]), high durability, mechanical/thermal/chemical stability, a robust synthetic route, and cost-effectiveness. It is challenging to fabricate AEMs with high OH^- ion conductivity and good mechanical properties;[3] increasing the ion exchange capacity (IEC) of the membrane improves the ion conductivity but is often accompanied by a

[a] *Integrated Graduate School of Medicine, Engineering, and Agricultural Sciences, University of Yamanashi, 4-3-37 Takeda, Kofu, Yamanashi 400-8510, Japan*
[b] *Hydrogen and Fuel Cell Nanomaterials Research Center, University of Yamanashi, 6-43 Miyamae, Kofu, Yamanashi 400-0021, Japan. E-mail: jinukai@yamanashi.ac.jp*
[c] *Clean Energy Research Center, University of Yamanashi, 4-3-11 Takeda, Kofu, Yamanashi 400-8510, Japan*
[d] *Department of Applied Chemistry, Waseda University, Tokyo 169-8555, Japan*

† Electronic supplementary information (ESI) available. See DOI: https://doi.org/10.1039/d3cp03660j

‡ Present address: LIB Technical Center, GS Yuasa International Ltd., 780-1, Hachiya, Ritto, Shiga 520-3021, Japan.

drop in the mechanical properties, such as increased swelling and brittleness.[3] Unlike $-SO_3H$ groups in proton exchange membranes (PEMs), such as Nafion®, anion-exchange groups do not strongly dissociate, and the electrochemical mobility of OH^- in water is lower than that of H^+. This results in lower ionic conductivities than those of commercial PEMs.[3] However, the biggest challenge for the practical application of AEMFCs is concurrently achieving a high power performance and cell durability.[5,8,9] Attempts to balance the mentioned factors have resulted in the development of several promising AEMs. Some of the recent developments are:

(i) LDPE-BTMA. This low-density polyethylene contains covalently bonded benzyl trimethyl-ammonium and cationic head groups. At a temperature of 80 °C and 95% relative humidity (RH), it has been reported to achieve an OH^- anion conductivity of 145 mS cm^{-1}.[10]

(ii) Ether-free AEMs (EF-AEM). These AEMs are prepared by superacid catalysis. Their membrane structure contains no ether group for better hydrolysis stability, better performance at elevated temperatures, and enhanced durability in fuel cells and electrolysers.[11–13] Ether-free polybenzimidazoles (PBIs) containing alicyclic and aliphatic segments have been reported to achieve OH^- anion conductivity of 108.8 mS cm^{-1} at 80 °C and a peak power density of 785 mW cm^{-2} at a current density of 1802.9 mA cm^{-2}.[13]

(iii) PiperION. This self-supporting membrane is manufactured from functionalised poly (aryl piperidinium) resin material without mechanical reinforcement. At a temperature of 80 °C and maximum hydration, it has been reported to achieve an OH^- anion conductivity of 148 mS cm^{-1}. At 60 °C, the peak power density of 442 mW cm^{-2} is reported.[14]

(iv) QPAF-4. This partially fluorinated AEM uses a quaternary ammonium group as the OH^- exchange site.[15] At temperatures of 80 °C, QPAF-4 with an IEC of 1.47 meq g^{-1} has been reported to achieve OH^- anion conductivity of up to 86.2 mS cm^{-1} with a roughly Arrhenius-type temperature dependence.[15]

The chemical structure of QPAF-4 is shown in Fig. 1. Attractive features of QPAF-4 include optimised ion exchange capacity, high hydroxide ion conductivity, excellent mechanical properties, and increased alkaline stability.[15] Otsuji *et al.*[16,17] have extensively studied AEMFCs using QPAF-4 as the AEM. From their reported results and other researchers who have used QPAF-4,[9,15–19] the application of QPAF-4 in experimental fuel cells has been well-established. Consequently, in the current research, we have selected QPAF-4 as the AEM to be studied first.

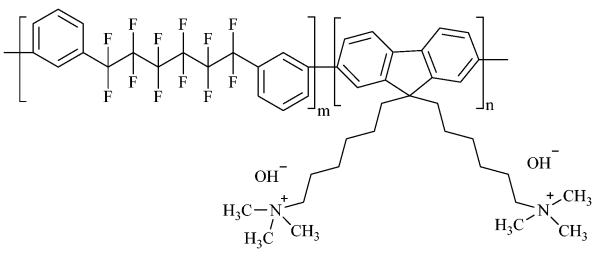

Fig. 1 Chemical structure of QPAF-4.

Regarding the intrinsic electrochemical reactions, an AEMFC produces twice as much water as a PEMFC at the anode and consumes water as a reactant at the cathode. This makes water management more complex than in a PEMFC. Besides, the conductivity of a typical AEM is known to drop sharply with decreasing water content.[20] Excess water at the anode of the AEMFC is partly removed through the anode discharge gas stream and partly by back-diffusion through the AEM to the cathode side.[21] On the other hand, a humidified feed air and fuel gas continuously supply additional water to the membrane during operation. With an appropriate understanding of the hydration requirements in AEMFCs, it could be possible to optimise their performance and achieve continuous AEMFC operation with no need for external humidification as has been established in commercial PEMFCs.[22,23] One method to eliminate the humidification requirement is using a water exchanger on the oxygen side of the cell to capture water from the discharge air and return the water to the inlet.[24] Another strategy is using ionomer binders in the catalyst layer with higher gas solubility than the AEM.[21] Modification of the GDL has also been proposed.[25] For the rapid and effective integration of these concepts in AEMFCs, it is beneficial to establish suitable techniques to study the water distribution inside the AEMs.

Several techniques are available for studying electrolyte membranes in running fuel cells, such as infrared spectroscopy,[26,27] coherent anti-Stokes Raman scattering (CARS) spectroscopy,[28–31] neutron imaging,[32–34] micro-Raman spectroscopy,[25,35,36] and combined calculations based on density functional theory (DFT) and vibrational spectroscopy.[37] Raman spectroscopy has the advantage of minimum modification of actual cells required, usage of less-damaging near-infrared radiation, high chemical sensitivity to both liquids and gases and high spatial resolution (approximately 5 μm) that permits analysis of the water-content distribution in the thin membranes.[36,38,39] In comparison to CARS, Raman has the advantage of being a well-established and easy-to-use technique because only one beam is used. It, therefore, serves as an excellent reference for new materials such as the QPAF-4 AEM studied in this paper.

Mattsson *et al.* used Raman spectroscopy to study the degradation of membranes.[40] They proved that the confocal Raman spectroscopy technique was suitable for investigating changes in membrane composition. Hara *et al.* used operando confocal micro-Raman spectroscopy to study the water distribution in a Nafion membrane in an operating fuel cell.[25,35] This technique made it possible to measure the hydration level at different membrane depths under diverse cell operation conditions, such as varied temperature, humidification, current density, and gas-flow rate. Kendrick *et al.* used operando Raman micro-spectroscopy to understand the polymer conformation of Nafion.[41]

Recently, Nishiyama *et al.* used CARS spectroscopy to elucidate the types of water species in Nafion.[29] Five different types

Table 1 Reported bands of interest in the deconvolution of water and alkalis

Serial number	Sbroscia *et al.*[47]	Pezzotti *et al.*[48]
1	3042–3200 cm^{-1}, Band I	3014 cm^{-1}, single donor double acceptor (DAA)
2	3220–3270 cm^{-1}, Band II	3226 cm^{-1}, double donor double acceptor (DDAA)
3	3393–3471 cm^{-1}, Band III	3432 cm^{-1}, single donor single acceptor (DA)
4	3546–3606 cm^{-1}, Band IV	3572 cm^{-1}, double donor single acceptor (DDA)
5	3612–3632 cm^{-1}, OH^-	3636 cm^{-1}, free OH/OH^-

of water were identified: water H-bonded to other water (3483 cm^{-1}), non-H-bonded water (3559 cm^{-1}), Eigen protonated water (3059 cm^{-1}), Zundel protonated water (3371 cm^{-1}) and water H-bonded to $-SO_3^-$ (3289 cm^{-1}).[29] To correctly interpret the spectroscopic parameters in an alkaline medium, it is mandatory to explicitly consider hydrogen bonding between the hydroxide and water molecules.[42] Several researchers have studied water molecules in alkaline solutions using Raman spectroscopy.[43–47] Corridoni *et al.*, while studying OH^- stretching band dynamics in LiOH, NaOH, and KOH solutions, were among the first to observe that five Gaussian bands were sufficient to describe the OH stretching region of the aqueous hydroxides.[45] Sbroscia *et al.*,[47] in a similar study in LiOH, NaOH, and KOH hydroxide solutions of different concentrations, also effectively used five bands identical to those reported by Corridoni *et al.* They selected Bands (I) to (IV) to best reproduce the O–H stretching region, while band V, located between 3610 and 3640 cm^{-1}, was ascribed to the hydroxide anion (Table 1).[47] Band IV (around 3557 cm^{-1}) was identified as a self-contribution of the correlation function. This view is based on the fact that Raman spectroscopy employs correlation functions of the derivative of molecular polarizability to probe molecular behaviour.[47] This function has two distinct contributions: inter-molecular interaction and self-contribution from single-molecule behaviour. They concluded that Bands I–III have a shared origin and a combined centre of gravity between 3290 and 3260 cm^{-1}. Pezzotti *et al.*, in a study on the effect of pH on the OH region, also observed that five bands represented the overall spectrum satisfactorily.[48] The five bands were labelled based on the donor/acceptor properties of water molecules, as listed in Table 1. Falk[49] and De Marco *et al.*,[50] using infrared spectra from O–^{1}H and O–^{2}H bond interactions, quite elaborately highlighted the accompanying molecular dynamics to this donor/acceptor phenomenon. Recently Wang *et al.* observed that the presence of KOH in water led to higher Raman intensity, the appearance of low-wavenumber Raman bands, and an enhanced hydrogen bonding network.[46]

It is expected that the full OH stretching band in any AEM should be a superposition of the vibrational contributions from H_2O, OH^-, vibrations unique to the AEM structure, and any interactions between the ions. For QPAF-4, based on its molecular structure, these expected bands in the OH region are:

(i) The hydroxide (OH^-) stretching band around 3600–3640 cm^{-1}.[44,45,47,51]

(ii) The bands for double donor single acceptor (DDA) H-bonded water, double donor double acceptor (DDAA) H-bonded water, single donor single acceptor (DA) H-bonded water, double donor single acceptor (DDA) H-bonded water, and free OH.[48,52,53]

(iii) The CH band from the benzene ring around 3000–3100 cm^{-1} [43,54,55] and the CH band from the methyl at the quaternary ammonia group around 2800–3000 cm^{-1}.[43,54]

(iv) Any interactions arising between the ions present.

The present study sought to quantify and characterise the water inside an AEM for the first time by Raman spectroscopy in an assembled cell at various RH values. The choice to use an assembled fuel cell is because this study is part of continuing research on water distribution in operational AEMFCs, despite no power generation being done in this study. The behaviour of the OH stretching band in alkaline solutions was first established. The findings from this exercise were used to complete the interpretation of the deconvoluted OH stretching region from the AEM. DFT calculations were carried out to shed further light on the interaction of various states of water in contact with the AEM.

2. Methodology

2.1. Experimental

As part of the assembly process, an airtight transparent quartz window 200 μm thick and 16 mm × 18 mm in size was mounted at the cathode end plate to allow the laser beam to access the gas diffusion layer (GDL) at the cathode side.[25,29–31,35] A pinhole of diameter 500 μm was punched at the centre of the GDL at the cathode side to allow laser light access to the QPAF-4 membrane. On the opposite side of the hole across the membrane, a thin Pt disk of diameter 500 μm was placed to reflect the Raman beam into the Raman microscope.[29–31] This beam was then directed into the spectrometer (see below). On the cathode side, the GDL used was 29BC from SGL Carbon Group Co. On the anode side, PANEX30 PW03 carbon cloth from Zoltek was used. Fig. 2 shows the exploded view of the Raman cell. No catalyst was used during the in-situ measurement reported in this paper. The thickness of the QPAF-4 AEM was 30 μm, and the IEC was 2.0 meq g^{-1}.[15]

Fig. 3 shows the system setup for Raman spectroscopy. The 633 nm laser was selected with a laser power of 1 mW. An objective lens with a magnification of ×50 was used with a 100 μm confocal aperture to illuminate the sample and collect the scattered Raman signal.

The absence of sample damage was confirmed by comparing the spectrum before and after 20 minutes of continuous

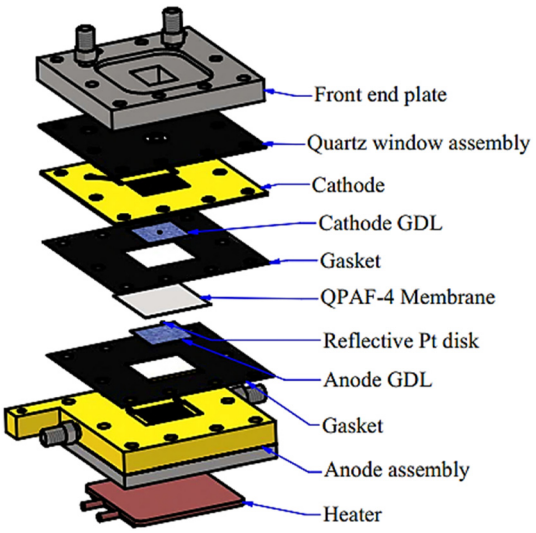

Fig. 2 Assembly of the fuel cell with a transparent quartz window, a hole in the GDL, and a reflective Pt disk.

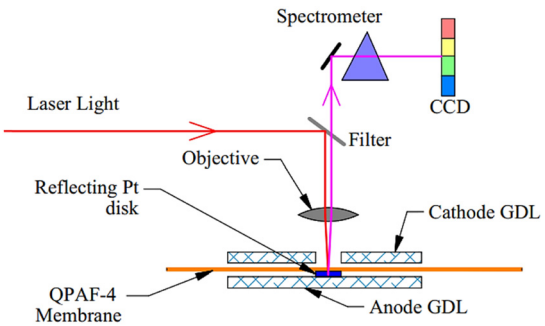

Fig. 3 Setup for micro-Raman spectroscopy. The red line shows the path of the 633 nm laser beam into the cell, and the pink line indicates the path followed by the generated signal into the spectrometer.

irradiation. A LabRAM HR-800 spectrometer from HORIBA Jobin Yvon Ltd with a charge-coupled device (CCD) detector was used to measure the spectra.

The exposure time was 15 s with five accumulations. The LabSpec5 software provided by Horiba was used for the baseline correction. The system was allowed to stabilise at each humidity for 3 hours before measurement.

2.2. DFT calculation

The DMol^3 DFT application was used[50,51] to carry out DFT calculations. First, the repeating section of the QPAF-4 structure was modelled, surrounded with water molecules, and structurally optimised. Vibrational frequency analysis was then carried out with Gaussian broadening to generate the spectrum. A detailed description of the procedure and parameters used is given in the ESI.†

3. Results and discussion

Fig. 4 shows the spectra of NaOH and KOH at various concentrations from 1.0 to 16 M on a silicon substrate. The spectra of

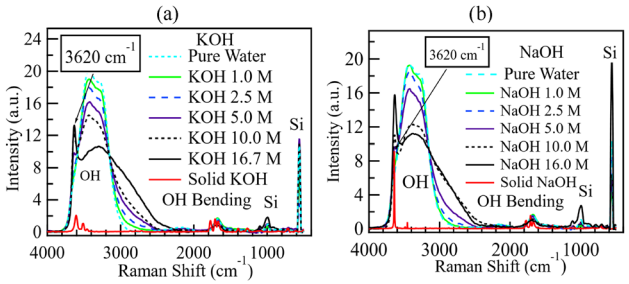

Fig. 4 Spectra from alkaline solutions of 0, 1.0, 2.5, 5.0, 10.0, and 16 M. (a) KOH and (b) NaOH. Apart from the dry alkali spectra, all the other spectra were normalised by the area between 2000 and 3800 cm^{-1}. The 0 M concentration points refer to the spectrum of pure water.

solid KOH (85 wt% with 15 wt% water, Fujifilm Pure Chem Corp.) and solid NaOH (97 wt% with 3% water, Fujifilm Pure Chem Corp.) heated to 110 °C to keep them dry are also shown. The Si–O bands from the silicon substrate were observed at 520 and 1000 cm^{-1}.[56,57] The solid KOH and NaOH spectra only showed peaks around 3600 cm^{-1} and 1450 cm^{-1}. Similar spectra are reported elsewhere.[58–60] The shape of the solid KOH peak around 3600 cm^{-1} is described as a doublet,[58] and its splitting is attributed to the coupling between the two OH$^-$ ions in the unit cell of KOH crystal.[58] In solutions, the HOH bending band appeared around 1650 cm^{-1},[51] and the OH stretching region was observed from 2500 to 3700 cm^{-1}.[61] A small sharp band emerged around 3620 cm^{-1} as the hydroxide concentration increased beyond 2.5 M. This sharp band has been assigned to the hydroxide ion,[47,48,51,62] and the broad shoulder around 2900 cm^{-1} to the hydroxide hydrate cluster.[51] At a low concentration of 1.0 M, the aqueous NaOH and KOH spectra were similar in shape to the spectrum obtained from pure water. However, the two hydroxide spectra quickly departed from that of pure water as the concentration increased, as shown in Fig. 4. It is also observed that there is almost complete absence of any broad shoulder around 2900 cm^{-1} in both the solid KOH/NaOH and pure water, yet the same feature appears when the hydroxides are diluted to 2.5–16 M. This further supports the assignment of the broad shoulder around 2900 cm^{-1} to hydrated hydroxide because it is the water-hydroxide interaction widely recognised by researchers whose primary structure is $H_3O_2^-$.[42,63–65]

The spectra of different concentrations of ammonium solutions on Si substrates were also obtained, as shown in Fig. 5. The Si–O bands from the silicon substrate were observed at 520 and 1000 cm^{-1},[56,57,66] as observed in the spectra for KOH and NaOH. As already stated, the HOH bending band was around 1650 cm^{-1}, and the OH stretching region was from 2500 to 3700 cm^{-1}.[61] A sharp band appeared within the OH region approximately at 3340 cm^{-1}. This band increased with the ammonia concentration and can be assigned to an N–H stretching band.[43] The concurrent appearance of this band with the O–H signal within the 2500–3700 cm^{-1} region suggests that any possible ammonia-water interactions in QPAF-4 would also be easily detectable.

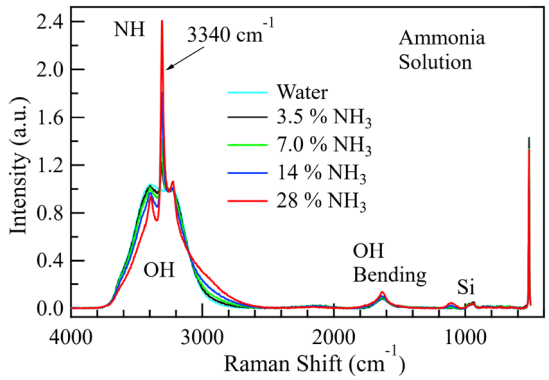

Fig. 5 The spectrum of water in 3.5, 7.0, 14, and 28 wt% ammonium solutions. Normalisation has been done using the area between 2000 and 3800 cm^{-1}.

As the ammonium hydroxide concentration increased beyond 14%, the OH band widened slightly around 3000 cm^{-1}. Unlike the case of KOH and NaOH solutions, a sharp OH^- band did not appear in the spectrum at 3620 cm^{-1}, suggesting that the influence of ammonium ion on the OH band could be different from that of the OH^- ion. Based on the spectra in Fig. 4 and 5, it is concluded that the OH region in the QPAF-4 AEM should capture (1) the hydroxide ion OH stretch if strongly alkaline and (2) the N–H band if present.

3.1. OH species in water

The OH region (2500–4000 cm^{-1}) was deconvoluted into five Gaussian bands in Fig. 6 as reported,[47,48,67,68] and the bands were labelled DAA, DDAA, DA, DDA, and free OH, where A refers to the acceptor and D to the donor species, as proposed by Sun.[69] The proposed band selection is also supported by other researchers.[48,52,70–72]

The bands at 3016, 3235, 3432, 3558, and 3658 cm^{-1} can be assigned to DAA H-bonded water,[48] DDAA H-bonded water,[48,69] DA H-bonded water,[48,69] DDA H-bonded water, and isolated water,[29,51,73] respectively. According to Sun,[69] DDAA and DA hydrogen-bonded water are the dominant H-bonding species in water under ambient conditions at a ratio of approximately 0.75 : 1. This dominance is confirmed in Fig. 6. No hydroxide band is expected at 3635 cm^{-1} for neutral samples, such as pure water. This deconvoluted spectrum for water was taken as the reference (0 M) for all the other aqueous solutions studied in this section.

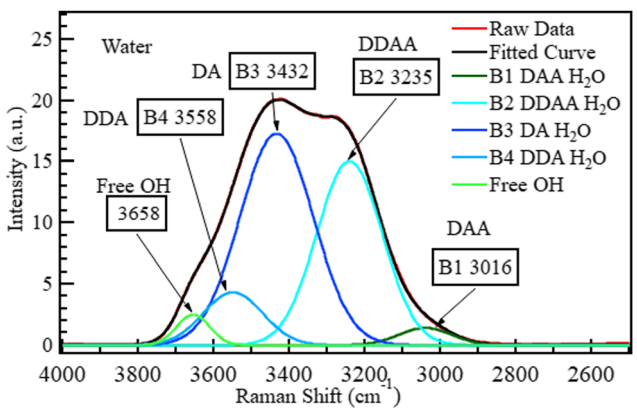

Fig. 6 The spectrum of liquid water deconvoluted into five Gaussian bands based on the Pezzotti assignments.[48] The raw data plot and fitted curve are also shown.

3.2. Behavior of the OH species in alkaline solutions

To establish the effect of variations in hydroxide concentration, the KOH and NaOH spectra in Fig. 4 were deconvoluted into seven bands, as shown in Fig. 7 Five for pure water[69] and two associated with alkaline solutions.[51] Fig. 7 and 8 show the deconvoluted bands of the highest and lowest KOH concentrations, respectively. The bands at 2900, 3018, 3238, 3434, 3555, 3600, and 3668 cm^{-1} can be assigned to $H_3O_2^-$, DAA, DDAA, DA, DDA H-bonded water, non-H-bonded OH and OH^- respectively. The bands are identical to the ones in water except for adding two bands unique to alkaline solutions at *ca.* 2900–2950 cm^{-1} and *ca.* 3620–3670 cm^{-1}.[51,59,63,74]

Fig. 7 and 8 show that the fraction of the $H_3O_2^-$ band corresponding to water H-bonded to OH^- increased sharply with KOH concentration from 1.0 to 16.0 M.

The areas of the bands in KOH at different concentrations are plotted in Fig. 9. The OH^- band intensity in Fig. 9 increased steadily with increasing KOH concentration, as expected. The $H_3O_2^-$ component similarly increased rapidly as the OH^- level grew to become the most significant fraction of the solution at 16.0 M. The band area contribution of $H_3O_2^-$ of only 2.7% at 1.0 M became 41% at 16.0 M, and the $H_3O_2^-$ component formed from OH^- became more significant than the OH^- component; OH^- ions are known to strongly H-bond with up to four H_2O molecules and weakly bond with a fifth one.[47] The two signals from OH^- and $H_3O_2^-$ were then attenuated by the same noise along the signal path, which further disadvantages the smaller signal, OH^-.

Although the presence of an alkaline solution has been found to lead to an enhanced H-bonding network in water,[46]

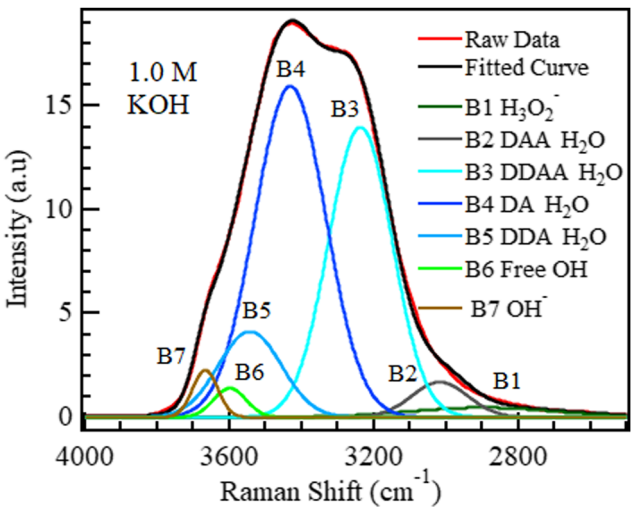

Fig. 7 1.0 M KOH spectrum deconvoluted into seven Gaussian bands.

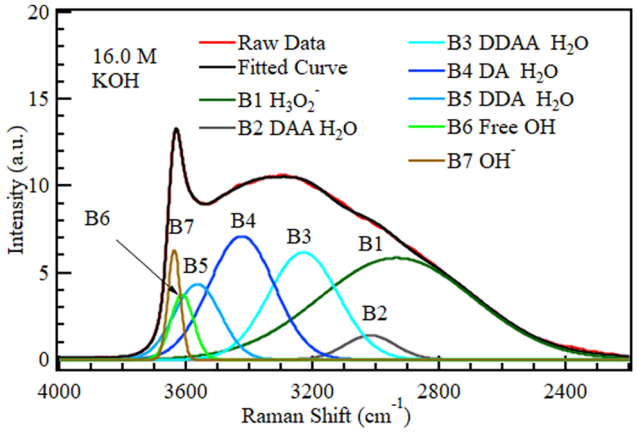

Fig. 8 16.0 M KOH spectrum deconvoluted into seven Gaussian bands.

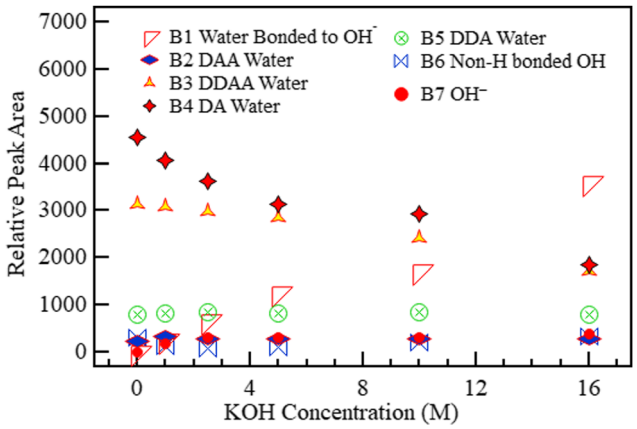

Fig. 9 The area under each of the five deconvoluted bands within the OH region of KOH with changing molar concentration. The 0 M concentration refers to the spectrum of pure water.

B6 (3600 cm^{-1}) in Fig. 9 representing non-H-bonded water[29,48,51,73] initially dropped slightly on the introduction of KOH at 1.0 M but then increased steadily with concentration almost to the initial level. This increase in non-H-bonded OH despite increased alkaline concentration suggests that there could be more than one origin of the non-H-bonded band. Walrafen *et al.* reported two distinct $H_3O_2^-$-related bands: one around 2950 cm^{-1} and the second at 3500–3596 cm^{-1}.[51] The location of this second $H_3O_2^-$ band is the same as that of B6 in Fig. 7 and 8. Since increased KOH concentration is accompanied by increased $H_3O_2^-$ clusters, this occurrence transitions the band from "standard" isolated OH (non-H-bonded OH in an H_2O molecule that only interacts with other water molecules) to a combination of the (1) "standard" isolated OH band and (2) O–H stretch of OH not directly H-bonded to OH^- within the $H_3O_2^-$ cluster.

The seven bands reproduced the original spectra in all cases, indicating that no new molecular clusters were formed in the solution. All the other H-bonded OH species (DAA, DDAA, DA, and DDA) decreased with increased KOH concentration

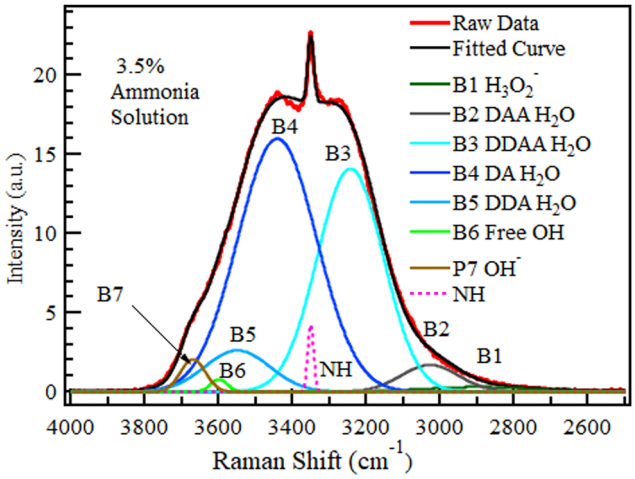

Fig. 10 Spectrum of 3.5 wt% NH_4OH deconvoluted into eight Gaussian bands.

because the formation of $H_3O_2^-$ clusters in the KOH solution required a combination of the existing H_2O, whose supply is fixed with OH^-. The NaOH spectra were also deconvoluted, and the results were like those reported for KOH, as shown in Fig. S1–S3 (ESI†).

The spectra of ammonium solution reported in Fig. 5 were likewise deconvoluted in Fig. 10 (3.5 wt%) and Fig. 11 (28 wt%). The variation in the quantity of each species with concentration is shown in Fig. 12. Fig. 11 and 12 show that a sharp rise in the NH band intensity accompanied the increase in ammonium solution concentration. As in the case of KOH and NaOH, the increase in solution concentration was accompanied by a decrease in DDAA and DA bands. Although the hydroxide band intensity increased slightly from 0% to 28% (maximum concentration at room temperature and pressure), the increase was negligible compared to the rise observed in NaOH and KOH because NH_4OH is a weak base, with the speciation being

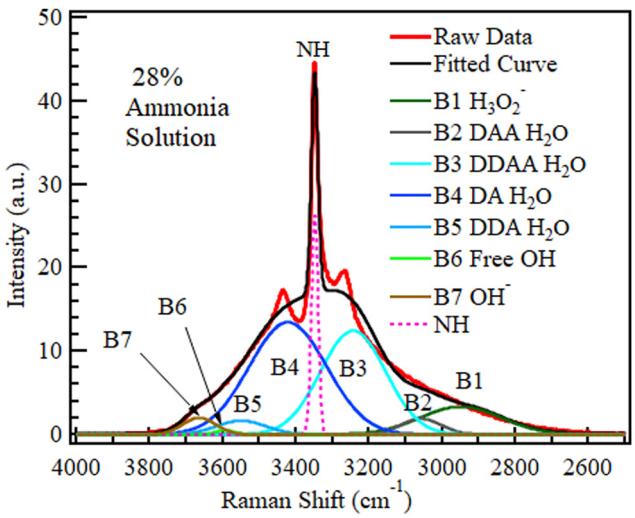

Fig. 11 Spectrum of 28 wt% NH_4OH deconvoluted into eight Gaussian bands.

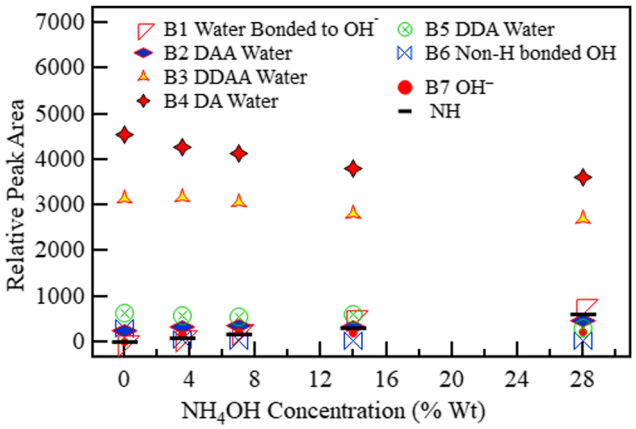

Fig. 12 The area under the six deconvoluted OH sub-bands within the OH band of aqueous NH_4OH with changing concentration. The 0 M concentration points refer to the spectrum of pure water.

mostly NH_3 and H_2O.[75,76] As a result, there is a relatively low OH^- concentration present. Therefore, B1 observed in Fig. 10 and 11 could have a contribution from both $H_3O_2^-$ and an NH_3–H_2O complex.[43] Fig. 8 and 11 show that OH^- results in a more prominent spread of the OH band towards the low wavenumber region than ammonia. Therefore, the effect of NH_3–H_2O on the OH region must be minimal.

Raman spectra of QPAF-4 at varying RH. Fig. 13 shows the Raman spectra recorded at the centre of the membrane at various RH values at a fixed cell temperature of 60 °C. Multiple bands between 500 and 2500 cm^{-1} are observed. These bands did not appear in the spectra of the aqueous solutions. Consequently, these modulations were attributed to wave interference from the membrane being measured. Three prominent bands were observed before deconvolution: (1) an OH band centred around 3200 cm^{-1}, (2) the aromatic stretch centred around 1620 cm^{-1}, and (3) the alkyl C–C stretch around 1300 cm^{-1}. The CH bond is also expected between 3000–3100 cm^{-1},[55,56] overlapping with the OH bands and requiring deconvolution to isolate it.

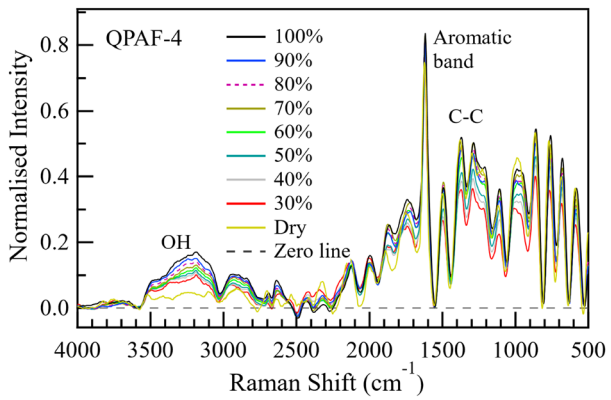

Fig. 13 Normalised Raman spectra from the centre of the QPAF-4 membrane at RH values 30–100% in steps of 10%. The spectra were normalised using the area under the aromatic band. A ×50 objective lens, 100 μm hole, and D1 filter were used during the measurements.

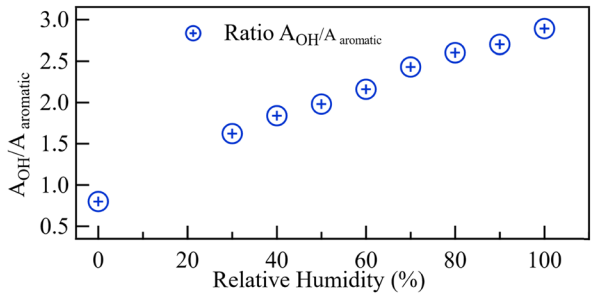

Fig. 14 The ratio of the OH stretching band area to that of the aromatic band from 30% to 100% RH at the centre of the QPAF-4 membrane.

The height of the OH bands increased with increasing RH. Fig. 14 plots the ratio of the total area under the OH bands to the area under the aromatic band. The area under the OH band increased with increasing RH nearly in the same linear manner previously reported for Nafion when operated at 60 °C.[25] Fig. S4 (ESI†) shows the water uptake by QPAF-4 as derived from gravimetric analysis. Fig. S5 (ESI†) is the corresponding calibration graph relating the area-ratio reported in this paper ($A_{OH}/A_{Aromatic}$) to λ, the number of water molecules per ammonia group in the QPAF-4 membrane.

3.3. Deconvolution of O–H stretching bands of QPAF-4

Based on the results and inferences on the species expected in QPAF-4 in the previous subsection, a nine Gaussian band deconvolution between 2900 and 3700 cm^{-1} was the minimum requirement to account for all the anticipated species in the OH region. Fig. S7 and S8 in the ESI† show an optimised structure from the DFT calculation and a simulated Raman spectrum. The calculations using a fragment of the QPAF-4 structure together with water molecules also showed how various bands can emerge in the OH region, even though these bands were not directly assignable to specific types of donor–acceptor interactions due to the small number of water molecules. Each class of D–A interactions included a range of H-bonding distances, which led to a range of vibrational frequencies. The calculations, however, indicated a high possibility of additional bands related to H_2O–OH^- interactions at around 2600 and 2300 cm^{-1} and ruled out the case of a water-ammonium interaction within the QPAF-4 membrane. This brought the final total number of possible bands to 11. Fig. 15 shows a pictorial modelling of these peaks. Fig. 16 shows the 11-band deconvolution of the OH region of the QPAF-4 spectrum at 30% RH. These 11 bands provide a reasonable fit to the QPAF-4 spectrum.

The bands at (1) 2370, (2) 2608, (3) 2880, (4) 2942, (5) 3091, (6) 3163, (7) 3187, (8) 3348, (9) 3470, (10) 3510 and (11) 3725 cm^{-1} were assigned to (1) OH interaction with OH^-, (2) second OH interaction with OH^-, (3) third OH interaction with OH^-, (4) C–H in the quaternary ammonium group, (5) C–H on the benzene rings, (6) DAA H-bonded water, (7) DDAA water, (8) DA water, (9) DDA water, (10) non-H-bonded water and (11) OH^-, respectively. No band position, height, or FWHM was constrained for this initial RH condition. However, considering

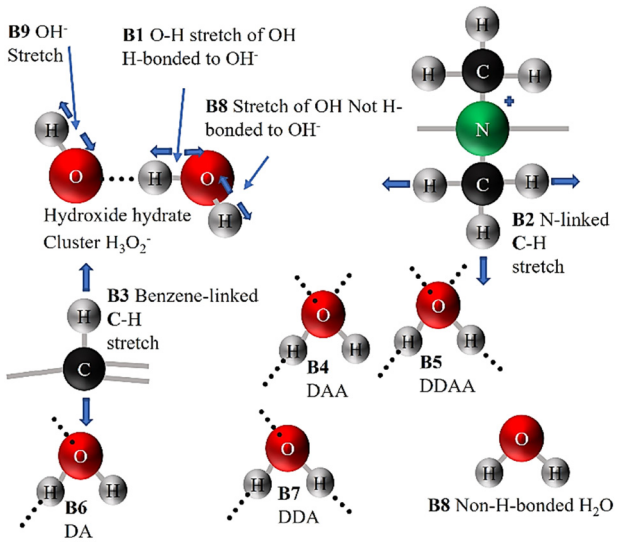

Fig. 15 A pictorial illustration of various structures in the OH region that contribute to the QPAF-4 spectrum. Covalent bonds are indicated using continuous lines, whereas weak hydrogen bonds/electrostatic interactions are shown as dashed lines.

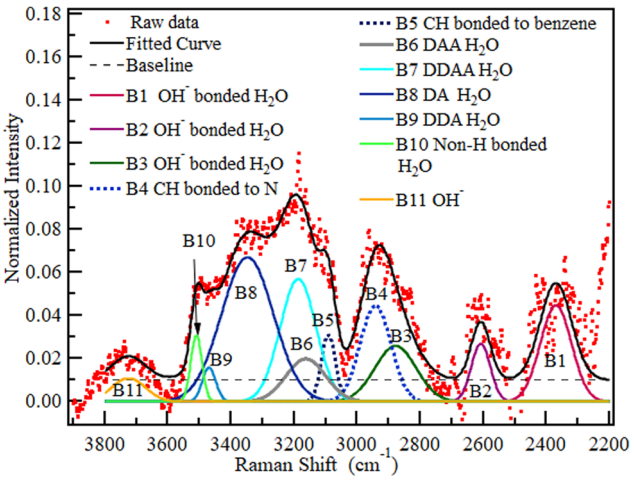

Fig. 16 The spectrum of QPAF-4 at 30% RH with deconvolution into eleven Gaussian bands with no constraints.

that, from Fig. 13, the first two bands, P1 and P2, observed in Fig. 16, bordered a region affected by wave interference, these two bands were ignored in comparing water at the various RH values. This decision is further supported by the fact that the same experiment has been redone using a newly developed CARS system at the University of Yamanashi, which will also be reported soon. Since the CARS signal suffered no such interference, it has been confirmed that the two low wavenumber bands in Fig. 16 were slightly affected by wave interference. The deconvolution in Fig. 17 below will thus be used to compare the water at various RH values.

The wavenumbers for the various bands remain as identified in Fig. 16, where bands (1) 2880, (2) 2942, (3) 3091, (4) 3163,

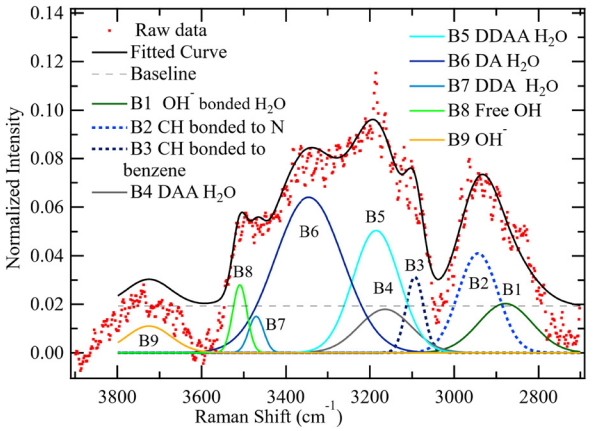

Fig. 17 The spectrum of QPAF-4 at 30% RH with deconvolution into nine Gaussian bands with no constraints.

(5) 3187, (6) 3348, (7) 3470, (8) 3510 and (9) 3725 cm^{-1} are assigned to (1) OH H-bonded directly to OH^-, (2) C–H in the ammonium group, (3) C–H on the benzene ring, (4) DAA H-bonded water, (5) DDAA water, (6) DA water, (7) DDA water (8) non-H-bonded water and (9) OH^-, respectively.

The deconvolution reported in Fig. 17 was carried out in a similar manner for all the other RH values from 40% to 100% RH. For this part of the deconvolution, the band position was constrained to be within ±10 cm^{-1} of the band location observed at 30% RH. The resulting $A_{OH}/A_{Aromatic}$ ratio for the nine species was plotted against RH in Fig. 18.

All the H-bonded species (water H-bonded to OH^- in $H_3O_2^-$, DAA water, DDAA water, DA water, and DDA water) increased with RH from 30% to 100%. The $H_3O_2^-$ band, however, levelled off after reaching 80% RH, showing saturation with four water molecules per ion. On the other hand, the bands without hydrogen bonds remained roughly constant with increasing RH. The constant bands are the two C–H bands (one in the methyl in the quaternary ammonium groups and the second in the benzene rings), the OH^- band, and the non-H-bonded OH band. Nishiyama *et al.* observed a band with similar traits at the same location (3500 cm^{-1}) in research on the chemical states of

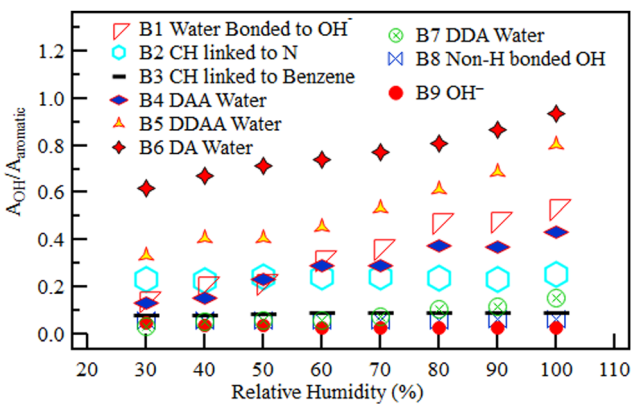

Fig. 18 The relative area under each of the nine deconvoluted OH sub-bands within the OH region of the QPAF-4 membrane with different RH.

water in Nafion.[29–31] They identified this as being non-H-bonded water. This band's behaviour suggests that the hydrophobicity of the aromatic rings and/or the C–F chains in the QPAF-4 structure also made it possible for some non-H-bonded OH groups to exist.

3.4. Comparison of QPAF-4 bands with PEM bands

For the case of Nafion, as reported by Nishiyama *et al.*, four unique types of water molecules were plotted: Eigen (3059 cm^{-1}) and Zundel (3371 cm^{-1}) protonated, H-bonded to the sulfonic acid group (3289 cm^{-1}), H-bonded to other water (3483 cm^{-1}), and non-H-bonded (3559 cm^{-1}).[29] They observed that only H-bonded species (two in number) increased with RH; protonated and non-H-bonded species remained constant with increasing RH.[29] Barique *et al.* also reported similar trends in the hydration number with variation in RH in Nafion using Fourier transform infrared spectroscopy.[27] These observations on H-bonded water species in PEMs agree with the results obtained in QPAF-4. However, all the species are different except for non-H bonded OH. This is because PEMs are acidic, with the SO_3^- counter-ion, while AEMs are alkaline. The OH region in PEMs only extends from around 3050 to 3550 cm^{-1}. In AEMs, the OH region extended past 3600 cm^{-1} to accommodate the OH^- band and spread to below 3000 cm^{-1} to accommodate the $H_3O_2^-$ band.

3.5. Effect of temperature on the spectra

The spectrum of the de-hydrated QPAF-4 membrane, previously dry purged with N_2 at 60 °C for 12 hours and placed on a silicon plate, was recorded at temperatures from 30 to 80 °C. At each temperature, the focal point was re-checked to ensure that the point was at the centre of the membrane. Fig. S6 (ESI†) shows the recorded spectra. No significant change in the relative size of peaks was observed in the spectrum. Chikaodinaka *et al.*, on the other hand, investigated the effect of temperature on the spectrum of fully immersed poly(diallyldimethylammonium).[77] They observed that in this fully hydrated form, a temperature change from 35 to 70 °C resulted in no change in the fingerprint region and a 20% reduction in the OH peak area.[77] From these two observations, it is concluded that since the cell temperature was constantly 60 °C during the reported experiments, the reported area ratio could be up to 20% less than that measured at temperatures of 45 °C below this value as observed by Chikaodinaka *et al.*[75] The possibility of this difference, however, was easily eliminated from our reported results by recording the water uptake graph used in calibration at the same cell temperature of 60 °C used when recording the spectra.

It must be mentioned that the temperature rise at the focal point resulting from laser heating of the membrane is by far the biggest thermal threat to the accuracy of the recorded spectrum. The resulting total/partial burnout from the laser can easily be noticed from the bend in the spectrum or visually through the microscope. Laser damage, however, manifests as a difference between the spectrum recorded at the beginning of the experiment and the one recorded at the end with the same parameter, particularly in the fingerprint region. For QPAF-4, laser heating was minimised by switching from a 514 nm laser to a 633 nm laser and reducing the beam power to 1 mW, whereas above 5 mW, laser damage was observed. Also, care must be taken to avoid excess fine carbon particles on the membrane surface in the observation area (such as those found in Pt catalysts on the carbon support) because these particles easily ignite when exposed to the high-intensity Raman laser.

3.6. Comparison of QPAF-4 with alkaline solution bands

In confined spaces such as a membrane, Raman bands are expected to undergo some displacement.[78]

Table 2. shows the displacement of bands in QPAF-4 compared to the same bands in the solution. The same phenomenon is, however, also observed in the alkaline spectrum as the concentration rises. An inspection of the data presented by researchers, such as Sbroscia *et al.*, also shows such band shifts in the alkaline band locations of up to 150 cm^{-1}.[47] This shift towards lower wavenumbers by up to 150 cm^{-1} in the OH region was attributed to the combined effect of liquid water confinement[69,78] and the enhanced H-bonding network in the alkaline environment.[46] This phenomenon in other AEMs will be studied in the future.

In this paper, we have intentionally omitted the plot of the actual number of water molecules for each species in the QPAF-4 membrane per quaternary ammonium group (λ). This is because, from the DFT calculation results, there are some water-related signals expected around 2300 and 2600 cm^{-1}, which have been left out of the analysis for the time being because of wave interference. Calculations of λ will therefore be addressed in more detail in future publications. However, briefly, the overall λ value for QPAF-4 at 40% RH was 1.3, out of which the largest water species, DA H-bonded water, contributes around 43%. At 80% RH, the overall λ was 5.6, of which

Table 2 Displacement of species in QPAF-4 compared to KOH solution spectrum

Band identity	16.0 M KOH band peak (cm^{-1})	QPAF-4 band peak (cm^{-1})	Change in wavenumber (cm^{-1})
$H_3O_2^-$	2935	2880	−55
C–H on NR_3 group	N/A	2942	N/A
C–H on benzene	N/A	3091	N/A
DDAA	3230	3187	−43
DA	3425	3348	−77
DDA	3565	3470	−95
Free OH	3613	3510	−103

DA contributes 33%. In comparison, Nafion at 40% and 80% RH exhibited overall λ values of 3.7 and 6.5, respectively.[29]

The λ value for QPAF-4 was 35% that of Nafion at 40% RH but increased rapidly with RH. At 80% RH, the λ value for QPAF-4 was 86% that of Nafion.

4. Conclusions

The micro-Raman spectroscopy technique was used to study different water species in AEM for the first time. The OH region was deconvoluted into nine bands (1) OH H-bonded to OH^-, (2) C–H bonded to the ammonium group as a methyl, (3) C–H on the benzene ring, (4) DAA H-bonded water, (5) DDAA H-bonded water, (6) DA H-bonded water (7) DDA H-bonded water, (8) non-H-bonded water and (9) the hydroxide anion. The band locations were very similar to those obtained from the DFT calculations. Apart from the two CH bands and non-H-bonded water, all the other band intensities increased with RH from 30% to 100%. The OH bands, however, generally appear to have shifted slightly towards the lower wavenumber region, a phenomenon caused by OH confinement and the enhanced hydrogen bonding in an alkaline medium. These findings open the path to extensive comparisons of the hydration characteristics of existing and new AEMs being developed. This will allow researchers to progressively build upon small improvements, resulting in enhanced ionic conductivity and a faster solution to the membrane durability problem facing AEMs.

Author contributions

Solomon W. Wakolo: Raman investigation, writing – original draft. Donald A. Tryk: DFT calculations, writing – review & editing. Hiromichi Nishiyama: experimental help, review. Kenji Miyatake: resources-AEM membrane preparation, review. Iiyama Akihiro: funding acquisition, review. Junji Inukai: supervision, conceptualization, funding acquisition, writing – review & editing.

Conflicts of interest

There are no conflicts to declare.

Acknowledgements

This work was supported by Grant-in-Aid for Scientific Research (No. 19K12632, 21H02044, 22K12673, and 23H2058) and Data Creation and Utilization Type Material Research and Development Project (JPMXP1122712807) from the Ministry of Education, Culture, Sports, Science and Technology-MEXT, by ECCEED'30 and ECCEED_GDL Projects from the New Energy and Industrial Technology Development Organization (NEDO), and by Yanmar Resource Circulation Support Organization.

References

1 H. Yang, Y. J. Han, J. Yu, S. Kim, S. Lee, G. Kim and C. Lee, Exploring Future Promising Technologies in Hydrogen Fuel Cell Transportation, *Sustainability*, 2022, **14**, 1–19.
2 R. Esbo, A. Ranjbar and S. Rahgoshay, Analysis of water management in PEM fuel cell stack at dead-end mode using direct visualization, *Renew. Energy*, 2020, **162**, 212–221.
3 C. Arges, V. Ramani and P. Pintauro, Anion Exchange Membrane Fuel Cells, *Electrochem. Soc. Interface*, 2010, **19**, 31–35.
4 R. Gutru, Z. Turtayeva, F. Xu, G. Maranzana, B. Vigolo and A. Desforges, *Int. J. Hydrogen Energy*, 2020, **45**, 19642–19663.
5 D. R. Dekel, Review of cell performance in anion exchange membrane fuel cells, *J. Power Sources*, 2018, **375**, 158–169.
6 J. C. Douglin, J. R. Varcoe and D. R. Dekel, A high-temperature anion-exchange membrane fuel cell, *J. Power Sources Adv.*, 2020, **5**, 100023.
7 A. R. Khade, Anion Exchange Membranes for Alkaline Fuel Cells Abnormal Situation Management View project Anion Exchange Membranes for Alkaline Fuel Cells, *Int. J. Sci. Res.*, 2015, **4**, 1406–1408.
8 J. R. Varcoe, P. Atanassov, D. R. Dekel, A. M. Herring, M. A. Hickner, P. A. Kohl, A. R. Kucernak, W. E. Mustain, K. Nijmeijer, K. Scott, T. Xu and L. Zhuang, Anion-exchange membranes in electrochemical energy systems, *Energy Environ. Sci.*, 2014, **7**, 3135–3191.
9 Y. Shirase, A. Matsumoto, K. L. Lim, D. A. Tryk, K. Miyatake and J. Inukai, Properties and Morphologies of Anion-Exchange Membranes with Different Lengths of Fluorinated Hydrophobic Chains, *ACS Omega*, 2022, **7**, 13577–13587.
10 L. Wang, J. J. Brink, Y. Liu, A. M. Herring, J. Ponce-González, D. K. Whelligan and J. R. Varcoe, Non-fluorinated pre-irradiation-grafted (peroxidated) LDPE-based anion-exchange membranes with high performance and stability, *Energy Environ. Sci.*, 2017, **10**, 2154–2167.
11 R. Ren, S. Zhang, H. A. Miller, F. Vizza, J. R. Varcoe and Q. He, Facile Preparation of an Ether-Free Anion Exchange Membrane with Pendant Cyclic Quaternary Ammonium Groups, *ACS Appl. Energy Mater.*, 2019, **2**, 4576–4581.
12 K. Min, Y. Lee, Y. Choi, O. J. Kwon and T. H. Kim, High-performance anion exchange membranes achieved by crosslinking two aryl ether-free polymers: poly(bibenzyl N-methyl piperidine) and SEBS, *J. Membr. Sci.*, 2022, **664**, 121071.
13 M. Guo, T. Ban, Y. Y. Wang, Y. Y. Wang, Y. Zhang, J. Zhang and X. Zhu, Exploring highly soluble ether-free polybenzimidazole as anion exchange membranes with long term durability, *J. Membr. Sci.*, 2022, **647**, 120299.
14 T. Novalin, D. Pan, G. Lindbergh, C. Lagergren, P. Jannasch and R. W. Lindström, Electrochemical performance of poly(arylene piperidinium) membranes and ionomers in anion exchange membrane fuel cells, *J. Power Sources*, 2021, **507**, 230287.
15 H. Ono, T. Kimura, A. Takano, K. Asazawa, J. Miyake, J. Inukai and K. Miyatake, Robust anion conductive

polymers containing perfluoroalkylene and pendant ammonium groups for high-performance fuel cells, *J. Mater. Chem. A*, 2017, **5**, 24804–24812.

16 K. Otsuji, N. Yokota, D. A. Tryk, K. Kakinuma, K. Miyatake and M. Uchida, Performance hysteresis phenomena of anion exchange membrane fuel cells using an Fe–N–C cathode catalyst and an in-house-developed polymer electrolyte, *J. Power Sources*, 2021, **487**, 229407.

17 K. Otsuji, Y. Shirase, T. Asakawa, N. Yokota, K. Nagase, W. Xu, P. Song, S. Wang, D. A. Tryk, K. Kakinuma, J. Inukai, K. Miyatake and M. Uchida, Effect of water management in membrane and cathode catalyst layers on suppressing the performance hysteresis phenomenon in anion-exchange membrane fuel cells, *J. Power Sources*, 2022, **522**, 230997.

18 J. Jiang, Z. Li, M. Xiao, S. Wang, K. Miyatake and Y. Meng, Quaternary ammonium-biphosphate ion-pair based copolymers with continuous H+ transport channels for high-temperature proton exchange membrane, *J. Membr. Sci.*, 2022, **660**, 120878.

19 K. Yoshida, T. Nagai, K. Ohara, Y. Shirase, K. Miyatake and J. Inukai, In-situ observation of an anion exchange membrane at various humidity by X-ray scattering, *J. Mol. Liq.*, 2023, **391**, 123197.

20 S. Gottesfeld, D. R. Dekel, M. Page, C. Bae, Y. Yan, P. Zelenay and Y. S. Kim, Anion exchange membrane fuel cells: Current status and remaining challenges, *J. Power Sources*, 2018, **375**, 170–184.

21 N. Ul Hassan, M. Mandal, G. Huang, H. A. Firouzjaie, P. A. Kohl and W. E. Mustain, Achieving High-Performance and 2000 h Stability in Anion Exchange Membrane Fuel Cells by Manipulating Ionomer Properties and Electrode Optimization, *Adv. Energy Mater.*, 2020, **10**, 2001986.

22 H. Yumiya, M. Kizaki and H. Asai, Toyota Fuel Cell System (TFCS), *World Electr. Veh. J.*, 2015, **7**, 85–92.

23 T. Yoshida and K. Kojima, Toyota MIRAI fuel cell vehicle and progress toward a future hydrogen society, *Electrochem. Soc. Interface*, 2015, **24**, 45–49.

24 J. Zhang, W. Zhu, T. Huang, C. Zheng, Y. Pei, G. Shen, Z. Nie, D. Xiao, Y. Yin and M. D. Guiver, Recent Insights on Catalyst Layers for Anion Exchange Membrane Fuel Cells, *Adv. Sci.*, 2021, **8**, 1–26.

25 M. Hara, J. Inukai, B. Bae, T. Hoshi, K. Miyatake, M. Uchida, H. Uchida and M. Watanabe, Micro-Raman study on water distribution inside a Nafion membrane during operation of polymer electrolyte fuel cell, *Electrochim. Acta*, 2012, **82**, 277–283.

26 E. A. Lewis, I. Kendrick, Q. Jia, C. Grice, C. U. Segre and E. S. Smotkin, Operando X-ray absorption and infrared fuel cell spectroscopy, *Electrochim. Acta*, 2011, **56**, 8827–8832.

27 M. A. Barique, E. Tsuchida, A. Ohira and K. Tashiro, Effect of Elevated Temperatures on the States of Water and Their Correlation with the Proton Conductivity of Nafion, *ACS Omega*, 2017, **3**, 349–360.

28 A. Syouji, M. Sakai, M. Hara and H. Matsushima, Drying process of water in a Nafion membrane embedded in the fuel cell analyzed by coherent anti-Stokes Raman scattering spectroscopy, *Jpn. J. Appl. Phys.*, 2018, **57**, 117101.

29 H. Nishiyama, S. Takamuku, K. Oshikawa, S. Lacher, A. Iiyama and J. Inukai, Chemical States of Water Molecules Distributed Inside a Proton Exchange Membrane of a Running Fuel Cell Studied by Operando Coherent Anti-Stokes Raman Scattering Spectroscopy, *J. Phys. Chem. C*, 2020, **124**, 9703–9711.

30 H. Nishiyama, S. Takamuku, A. Iiyama and J. Inukai, Dynamic Distribution of Chemical States of Water inside a Nafion Membrane in a Running Fuel Cell Monitored by Operando Time-Resolved CARS Spectroscopy, *J. Phys. Chem. C*, 2020, **124**, 19508–19513.

31 H. Nishiyama, A. Iiyama and J. Inukai, The distribution and diffusion coefficient of water inside a Nafion® membrane in a running fuel cell under transient conditions analyzed by operando time-resolved CARS spectroscopy, *J. Power Sources Adv.*, 2022, **13**, 100080.

32 Y. S. Chen, H. Peng, D. S. Hussey, D. L. Jacobson, D. T. Tran, T. Abdel-Baset and M. Biernacki, Water distribution measurement for a PEMFC through neutron radiography, *J. Power Sources*, 2007, **170**, 376–386.

33 J. Lee, H. D. Nguyen, S. Escribano, F. Micoud, S. Rosini, A. Tengattini, D. Atkins, G. Gebel, C. Iojoiu, S. Lyonnard and A. Morin, Neutron imaging of operando proton exchange membrane fuel cell with novel membrane, *J. Power Sources*, 2021, **496**, 229836.

34 M. Nasu, H. Yanai, N. Hirayama, H. Adachi, Y. Kakizawa, Y. Shirase, H. Nishiyama, T. Kawamoto, J. Inukai, T. Shinohara, H. Hayashida and M. Watanabe, Neutron imaging of generated water inside polymer electrolyte fuel cell using newly-developed gas diffusion layer with gas flow channels during power generation, *J. Power Sources*, 2022, **530**, 231251.

35 M. Hara, J. Inukai, K. Miyatake, H. Uchida and M. Watanabe, Temperature dependence of the water distribution inside a Nafion membrane in an operating polymer electrolyte fuel cell. A micro-Raman study, *Electrochim. Acta*, 2011, **58**, 449–455.

36 Y. Tabuchi, R. Ito, S. Tsushima and S. Hirai, Analysis of in situ water transport in Nafion® by confocal micro-Raman spectroscopy, *J. Power Sources*, 2011, **196**, 652–658.

37 S. B. Smedley, T. J. Zimudzi, Y. Chang, C. Bae and M. A. Hickner, Spectroscopic Characterization of Sulfonate Charge Density in Ion-Containing Polymers, *J. Phys. Chem. B*, 2017, **121**, 11504–11510.

38 A. Martinelli, C. Iojoiu and N. Sergent, A H 2/O 2 fuel cell for in situ μ-Raman measurements. In-depth characterization of an ionic liquid filled Nafion membrane, *Fuel Cells*, 2012, **12**, 169–178.

39 E. Cordero, F. Korinth, C. Stiebing, C. Krafft, I. W. Schie and J. Popp, Evaluation of shifted excitation Raman difference spectroscopy and comparison to computational background correction methods applied to biochemical Raman spectra, *Sensors*, 2017, **17**, 1724.

40 B. Mattsson, H. Ericson, L. M. Torell and F. Sundholm, Degradation of a fuel cell membrane, as revealed by micro-Raman spectroscopy, *Electrochim. Acta*, 2000, **45**, 1405–1408.

41 I. Kendrick, J. Fore, J. Doan, N. Loupe, A. Vong, N. Dimakis, M. Diem and E. S. Smotkin, Operando Raman Micro-Spectroscopy of Polymer Electrolyte Fuel Cells, *J. Electrochem. Soc.*, 2016, **163**, H3152–H3159.
42 M. V. Vener, I. G. Shenderovich and A. A. Rykounov, A qualitative study of the effect of a counterion and polar environment on the structure and spectroscopic signatures of a hydrated hydroxyl anion, *Theor. Chem. Acc.*, 2013, **132**, 1361.
43 T. Ujike and Y. Tominaga, Raman spectral analysis of liquid ammonia and aqueous solution of ammonia, *J. Raman Spectrosc.*, 2002, **33**, 485–493.
44 H. Kanno and J. Hiraishi, A Raman Study of Aqueous KOH Solution in Glassy State, *Bull. Chem. Soc. Jpn.*, 1985, **58**, 2701–2702.
45 T. Corridoni, A. Sodo, F. Bruni, M. A. Ricci and M. Nardone, Probing water dynamics with OH-, *Chem. Phys.*, 2007, **336**, 183–187.
46 Y. Wang, F. Li, C. Wang, W. Fang, C. Sun and Z. Men, Enhanced stimulated Raman scattering of water by KOH, *Opt. Express*, 2020, **28**, 9533.
47 M. Sbroscia, A. Sodo, F. Bruni, T. Corridoni and M. A. Ricci, OH Stretching Dynamics in Hydroxide Aqueous Solutions, *J. Phys. Chem. B*, 2018, **122**, 4077–4082.
48 G. Pezzotti, L. Puppulin, A. La Rosa, M. Boffelli, W. Zhu, B. J. H. S. McEntire, T. Nakahari and Y. Marunaka, Effect of pH and monovalent cations on the Raman spectrum of water: Basics revisited and application to measure concentration gradients at water/solid interface in Si3N4 biomaterial, *Chem. Phys.*, 2015, **463**, 120–136.
49 M. Falk, An infrared study of water in perfluorosulfonate (Nafion) membranes, *Can. J. Chem.*, 1980, **58**, 1495–1501.
50 L. De Marco, W. Carpenter, H. Liu, R. Biswas, J. M. Bowman and A. Tokmakoff, Differences in the Vibrational Dynamics of H2O and D2O: Observation of Symmetric and Antisymmetric Stretching Vibrations in Heavy Water, *J. Phys. Chem. Lett.*, 2016, **7**, 1769–1774.
51 G. E. Walrafen and R. T. W. Douglas, Raman spectra from very concentrated aqueous NaOH and from wet and dry, solid, and anhydrous molten, LiOH, NaOH, and KOH, *J. Chem. Phys.*, 2006, **124**, 114504.
52 Q. Sun and Y. Guo, Vibrational sum frequency generation spectroscopy of the air/water interface, *J. Mol. Liq.*, 2016, **213**, 28–32.
53 Q. Sun and H. Zheng, Raman OH stretching vibration of ice Ih, *Prog. Nat. Sci.*, 2009, **19**, 1651–1654.
54 C. Minejima, T. Ebata and N. Mikami, C-H stretching vibrations of benzene and toluene in their S1 states observed by double resonance vibrational spectroscopy in supersonic jets, *Phys. Chem. Chem. Phys.*, 2002, **4**, 1537–1541.
55 N. Zhang, Z. J. Tian, Y. Y. Leng, H. T. Wang, F. Q. Song and J. H. Meng, Raman characteristics of hydrocarbon and hydrocarbon inclusions, *Sci. China, Ser. D Earth Sci.*, 2007, **50**, 1171–1178.
56 Raman Spectroscopy for Analysis and Monitoring, Horiba Jobin Yvon, 2017.
57 V. V. Kidalov, S. A. Kukushkin, A. V. Osipov, A. V. Redkov, A. S. Grashchenko, I. P. Soshnikov, M. E. Boiko, M. D. Sharkov and A. F. Dyadenchuk, Growth of SiC films by the method of substitution of atoms on porous Si (100) and (111) substrates, *Mater. Phys. Mech.*, 2018, **36**, 39–52.
58 R. G. Snyder, J. Kumamoto and J. A. Ibers, Vibrational spectrum of crystalline potassium hydroxide, *J. Chem. Phys.*, 1960, **33**, 1171–1177.
59 Infrared spectrum of potassium hydroxide, **https://www.chemicalbook.com/SpectrumEN_1310-58-3_IR1.htm**.
60 Infrared spectrum of sodium hydroxide, **https://www.chemicalbook.com/SpectrumEN_1310-73-2_IR1.htm**.
61 T. Li, F. Li, Z. Li, C. Sun, J. Tong, W. Fang and Z. Men, Influence of strong and weak hydrogen bonds in ices on stimulated Raman scattering, *Opt. Lett.*, 2016, **41**, 1297.
62 A. Mandal and A. Tokmakoff, Vibrational dynamics of aqueous hydroxide solutions probed using broadband 2DIR spectroscopy, *J. Chem. Phys.*, 2015, **143**, 194501.
63 H. M. Lee, P. Tarkeshwar and K. S. Kim, Structures, energetics, and spectra of hydrated hydroxide anion clusters, *J. Chem. Phys.*, 2004, **121**, 4657–4664.
64 Y. Ogata, Y. Kawashima, K. Takahashi and M. Tachikawa, Is the structure of hydroxide dihydrate OH−(H2O)2? An ab initio path integral molecular dynamics study, *Theor. Chem. Acc.*, 2015, **134**, 1–6.
65 D. Peláez and H. D. Meyer, On the infrared absorption spectrum of the hydrated hydroxide (H3O2-) cluster anion, *Chem. Phys.*, 2017, **482**, 100–105.
66 D. Wolf, V. Senez, R. Balboni, A. Armigliato, S. Frabboni, A. Cedola and S. Lagomarsino, Techniques for mechanical strain analysis in sub-micrometer structures: TEM/CBED, micro-Raman spectroscopy, X-RAY micro-diffraction and modeling, *Microelectron. Eng.*, 2003, **70**, 425–435.
67 Q. Sun and C. Qin, Raman OH stretching band of water as an internal standard to determine carbonate concentrations, *Chem. Geol.*, 2011, **283**, 274–278.
68 P. Laurson, P. Raudsepp, H. Kaldmäe, A. Kikas and U. Mäeorg, The deconvolution of FTIR-ATR spectra to five Gaussians for detection of small changes in plant-water clusters, *AIP Adv.*, 2020, **10**, 85214.
69 Q. Sun, The single donator-single acceptor hydrogen bonding structure in water probed by Raman spectroscopy, *J. Chem. Phys.*, 2010, **132**, 10–14.
70 N. Kitadai, T. Sawai, R. Tonoue, S. Nakashima, M. Katsura and K. Fukushi, Effects of ions on the oh stretching band of water as revealed by atr-ir spectroscopy, *J. Solution Chem.*, 2014, **43**, 1055–1077.
71 W. J. Smit, F. Tang, Y. Nagata, M. A. Sánchez, T. Hasegawa, E. H. G. Backus, M. Bonn and H. J. Bakker, Observation and Identification of a New OH Stretch Vibrational Band at the Surface of Ice, *J. Phys. Chem. Lett.*, 2017, **8**, 3656–3660.
72 D. Li, Z. Zhu and D. W. Sun, Quantification of hydrogen bonding strength of water in saccharide aqueous solutions by confocal Raman microscopy, *J. Mol. Liq.*, 2021, **342**, 117498.

73 M. Ferrari, J. Catalano, M. G. Baschetti, M. G. De Angelis, G. C. Sarti, I. Chimica, A. Dicma and A. M. Studiorum-universita, Membrane, *Macromolecules*, 2012, **45**, 1901–1912.
74 M. Morita and K. Takahashi, Ionic Hydrogen Bonding Vibration in $OH^{-}(H2O)2\_4$, *J. Comput. Chem.*, 2016, **15**, 192–198.
75 J. G. Southwick, E. Van Den Pol, C. H. T. Van Rijn, D. W. Van Batenburg, D. Boersma, Y. Svec, A. A. Mastan, G. Shahin and K. Raney, Ammonia as alkali for alkaline/surfactant/polymer floods, *SPE J.*, 2015, **21**, 10–21.
76 R. G. Bates and G. D. Pinching, Dissociation Constant of Aqueous Ammonia, *J. Am. Chem. Soc.*, 1950, **72**, 1393–1396.
77 M. B. Chikaodinaka Eneha, P. Suarez-Martinez, A. Bachmannb, T. Zimudzic, M. Hickner, P. Batysd, M. Sammalkorpie and J. Lutkenhaus, Fourier Transform Infrared Spectroscopy Investigation of Water Microenvironments in Polyelectrolyte Multilayers at Varying Temperatures, *Soft Matter.*, 2020, 2291–2300.
78 R. Zangi and A. E. Mark, Electrofreezing of confined water, *J. Chem. Phys.*, 2004, **120**, 7123–7130.

